



Article

Asymmetric Schottky Barrier-Generated MoS₂/WTe₂ FET Biosensor Based on a Rectified Signal

Xinhao Zhang ^{1,†}, Shuo Chen ^{1,†}, Heqi Ma ¹, Tianyu Sun ¹, Xiangyong Cui ¹, Panpan Huo ¹, Baoyuan Man ^{1,*} and Cheng Yang ^{1,2,*}

¹ School of Physics and Electronics, Shandong Normal University, Jinan 250014, China; zhangxh0050@163.com (X.Z.); shuochen1119@gmail.com (S.C.); heqima9@163.com (H.M.); s15169093367@126.com (T.S.); CXY2023025549@outlook.com (X.C.); hpp6780@163.com (P.H.)

² Shandong Provincial Engineering and Technical Center of Light Manipulations, Shandong Normal University, Jinan 250014, China

* Correspondence: byman@sdnu.edu.cn (B.M.); chengyang@sdnu.edu.cn (C.Y.)

[†] These authors contributed equally to this work.

Abstract: Field-effect transistor (FET) biosensors can be used to measure the charge information carried by biomolecules. However, insurmountable hysteresis in the long-term and large-range transfer characteristic curve exists and affects the measurements. Noise signal, caused by the interference coefficient of external factors, may destroy the quantitative analysis of trace targets in complex biological systems. In this report, a “rectified signal” in the output characteristic curve, instead of the “absolute value signal” in the transfer characteristic curve, is obtained and analyzed to solve these problems. The proposed asymmetric Schottky barrier-generated MoS₂/WTe₂ FET biosensor achieved a 10⁵ rectified signal, sufficient reliability and stability (maintained for 60 days), ultra-sensitive detection (10 aM) of the Down syndrome-related DYRK1A gene, and excellent specificity in base recognition. This biosensor with a response range of 10 aM–100 pM has significant application potential in the screening and rapid diagnosis of Down syndrome.

Keywords: Schottky junction; field-effect transistor; biosensor; rectified signal; ultra-sensitive detection



Citation: Zhang, X.; Chen, S.; Ma, H.; Sun, T.; Cui, X.; Huo, P.; Man, B.; Yang, C. Asymmetric Schottky

Barrier-Generated MoS₂/WTe₂ FET Biosensor Based on a Rectified Signal. *Nanomaterials* **2024**, *14*, 226. <https://doi.org/10.3390/nano14020226>

Academic Editors: Filippo Giannazzo, Simonpietro Agnello, Luca Seravalli and Federica Bondino

Received: 20 December 2023

Revised: 9 January 2024

Accepted: 14 January 2024

Published: 20 January 2024



Copyright: © 2024 by the authors. Licensee MDPI, Basel, Switzerland. This article is an open access article distributed under the terms and conditions of the Creative Commons Attribution (CC BY) license (<https://creativecommons.org/licenses/by/4.0/>).

1. Introduction

Low-dimensional materials-based field-effect transistor (FET) biosensors have the advantages of high sensitivity, fast detection, miniaturization, low cost, and compatibility with integrated circuits [1–3]. However, the commonly used signals in FET biosensors are referred to as “absolute value signals”. These include Dirac voltage, threshold voltage V_{th} , source-drain current I_{ds} , and others [4–7]. These “absolute value signals” directly collect and process the specific changes in biomolecules. Although these signals carry the biomolecules’ charge information [8–10], they have the drawbacks of incomplete, unstable, and unreliable detection. Kulkarni et al. reported that the detection range of FET-based biosensors was limited by the Debye length due to the Debye screening effect. Consequently, molecular charge information outside the Debye length cannot be detected [11]. Sadighbayan et al. reported that ions in water or an electrolyte solution affected the surface potential or electric field of the sensor, causing fluctuations in the “absolute value signal”. The fluctuations made the stable detection of the charge information of biomolecules challenging [12]. Xu et al. reported that non-target molecules on the sensor surface can generate non-specific signals, affecting the charge density or potential on the sensor surface. This non-specific signal makes the detected “absolute value signal” unreliable [13,14].

A series of signal optimization models and signal processing methods for the “absolute value signals” have been proposed by researchers to accurately express the charge information carried by biomolecules. Fathi-Hafshejani, Parvin and coworkers combined

density functional theory (DFT) and the collected “absolute value signals”. They optimized the calculation model of the interaction energy and charge transfer between MUA (mercaptoundecanoic acid) and WSe₂, achieving the rapid and sensitive detection of the novel coronavirus (SARS-CoV-2) [15]. By adding a MoS₂ layer on graphene, Chen et al. suppressed the interference caused by the Debye screening effect on charge information detection. Consequently, they achieved the high integrity of charge information detection under physiological environment conditions [16]. Hajian, Reza et al. used the double exponential function and linear regression model to determine the relationship between the signal change curve and DNA concentration, and then cross-checked the theoretical results with the experimental “absolute value signals” to improve the detection stability [17]. Sarah Balderston et al. identified an insurmountable hysteresis phenomenon in measuring the transfer characteristic curve. They proposed a signal-processing model based on the average transconductance of small-range scanning gate voltage to minimize the interference of the hysteresis phenomenon on the measurement results, achieving single-base mutation detection in the BRCA1 and KRAS genes [18]. These models and strategies have significantly promoted signal accuracy. However, due to the inherent defects of the sensing materials, measurements still suffer from the interference of the hysteresis phenomenon while determining the influence of biomolecules on the intrinsic electric field of the sensing materials.

This study, for the first time, reports a strategy of using a “rectified signal” in the output characteristic curve instead of the “absolute value signal” in the transfer characteristic curve. A Schottky barrier-based MoS₂/WTe₂ FET biosensor was prepared to generate a “rectified signal” in the output characteristic curve. The low work function semimetal WTe₂ electrode replaced the Au electrode and formed a Schottky junction with MoS₂, reducing the Schottky barrier height at the WTe₂/MoS₂ interface and increasing carrier mobility. The Schottky barrier difference between the WTe₂/MoS₂ electrode and MoS₂/Au electrode caused the rectification ratio. Furthermore, the MoS₂/WTe₂ FET biosensor was used as a sensing platform to detect the Down syndrome-related DYRK1A gene, achieving a detection limit of 10 aM and high specificity. The linear response range was 10 aM–100 pM, indicating that the MoS₂/WTe₂ FET biosensor has broad application potential in the screening and rapid diagnosis of Down syndrome.

2. Materials and Methods

2.1. Materials

PBS (pH~7.0–7.2), 1-pyrenebutanoic acid succinimidyl ester (PBASE), DMSO, and ethanolamine were procured from Aladdin Co., Ltd. (Shanghai, China). SiO₂/Si substrates, bulk MoS₂, 1T'-WTe₂, blue film tape, and PDMS (polydimethylsiloxane) film were purchased from Shanghai Onway Technology Co., Ltd. (Shanghai, China). Other reagents were procured from Sinopharm Chemical Reagent Co., Ltd. (Shanghai, China). Deionized water (DI water) was collected from a Millipore water purification system (Milli-Q Direct8). The partial DNA/RNA sequences were purchased from Sangon Biotech (Shanghai) Co., Ltd. (Shanghai, China) (Table S1).

2.2. Device Fabrication

MoS₂ and 1T'-WTe₂ films were peeled off from their crystal blocks using blue film tape and then transferred to the PDMS film using a two-dimensional material transfer platform. Finally, MoS₂ and 1T'-WTe₂ films with the optimal thickness, size, and morphology were transferred to the SiO₂/Si substrates with pre-lithographed electrodes, forming 1T'-WTe₂/MoS₂ devices (Figure S1).

2.3. Device Functionalization and Immobilization

Before the detection of the target DNA molecule, the constructed MoS₂/WTe₂ needed to be functionalized and immobilized. PBASE was selected to functionalize MoS₂ and immobilize the probe DNA as a linker between MoS₂ and probe DNA. PBASE, when

dissolved in DMSO, stacks its pyrene group on the surface of MoS₂, binds to MoS₂, and immobilizes the probe DNA via the coupling reaction between the amine of the probe DNA and the amine-reactive succinimide group of PBASE (Figure S2). During functionalization, the PBASE solution, placed in an Eppendorf tube (EP tube), reacted with the MoS₂/WTe₂ FET biosensor at 37 °C for 20 min in a constant temperature box to deposit the pyrene groups in PBASE on the MoS₂ surface by π - π stacking. After reaction completion, the unreacted samples on the surface were washed off with DMSO solution. During the probe DNA immobilization, the probe DNA solution (1 pM) was placed in an EP tube and reacted with the MoS₂/WTe₂ FET biosensor at 37 °C for 2 h in a constant temperature box to immobilize the probe DNA via a conjugation reaction between the amine group of the probe DNA and the amine-reactive succinimide group of PBASE. The shift of the Mo3d peak and S2p peak positions confirmed that PBASE and the probe DNA were successfully combined on the MoS₂/WTe₂ surface (Figure S3). After reaction completion, the unreacted gene samples on the surface were washed off with 1×PBS solution. In the target DNA detection process, 200 μ L of the DYRK1A gene sample was placed in an EP tube, followed by a reaction with the MoS₂/WTe₂ FET biosensor at 37 °C for 2 h in a constant temperature box to allow more target DNA to diffuse to the MoS₂ surface and be captured by the probe DNA on the surface. After completion, the unreacted gene samples on the surface were washed off with 1×PBS solution, and the performance of the MoS₂/WTe₂ FET biosensor was tested after drying.

2.4. Characterization

The electrical properties of the MoS₂/WTe₂ FET biosensor were determined using a Keithley 4200-SCS semiconductor parameter analyzer at room temperature and in atmospheric pressure, dry, dark, and well-ventilated conditions. A constant stride interval of 20 mV was applied to the V_{DS}-I_{DS} curve. The structure and morphologies of the prepared samples were analyzed using SEM (Zeiss Gemini Ultra-55, 3.0 kV, Oberkochen, Germany) and EDS. AFM was used to determine the roughness of the MoS₂/WTe₂ surface. The Raman spectrometer used in this study was a Horiba HR Evolution 800 with a 532 nm excitation laser. The XPS characterization was conducted using a Thermo Fisher Scientific Escalab 250Xi instrument (Waltham, MA, USA) with an Al K X-ray source at 150 W and a spot size of 500. The spectra were acquired with an operating voltage of 12.5 kV and a spectrometer pressure of 8×10^{-10} mbar. The XPS spectra were calibrated by the peak of C 1s at 282 eV, normalized by the baseline level, and curve-fitted by smart function.

3. Results and Discussion

3.1. The Advantages and Generation Mechanisms of the Rectified Signal

The rectified signal is a kind of response signal, which is composed of two currents with opposite directions. It effectively reflects the specific changes in the biomolecules. Taking the current variation (ΔI) and rectification ratio variation (ΔR) as examples, the accuracy of the “absolute value signal” and “rectified signal” can be discussed in detail.

Figure 1A shows that, when the “absolute value signal” (such as source-drain current) is used as the response signal, which can be expressed as [19]

$$\Delta I = I_2 - I_1, \quad (1)$$

I_1 and I_2 are the measured source-drain currents at different biomolecular concentrations.

$$I_1 = C_1 \cdot I_{1.\text{True}}; I_2 = C_2 \cdot I_{2.\text{True}}, \quad (2)$$

$I_{1.\text{True}}$ and $I_{2.\text{True}}$ are the accurate values of the source-drain current at different biomolecular concentrations without interference from external factors. The constant C_i ($i = 1, 2$) represents the interference coefficient of external factors at different biomolecular concentrations. Since I_2 and I_1 are “absolute value signals” at different biomolecular concentrations, each external factor affects them differently ($C_2 \neq C_1$), which implies that

the charge information carried by biomolecules cannot be accurately determined by using an “absolute value signal” as a response signal.

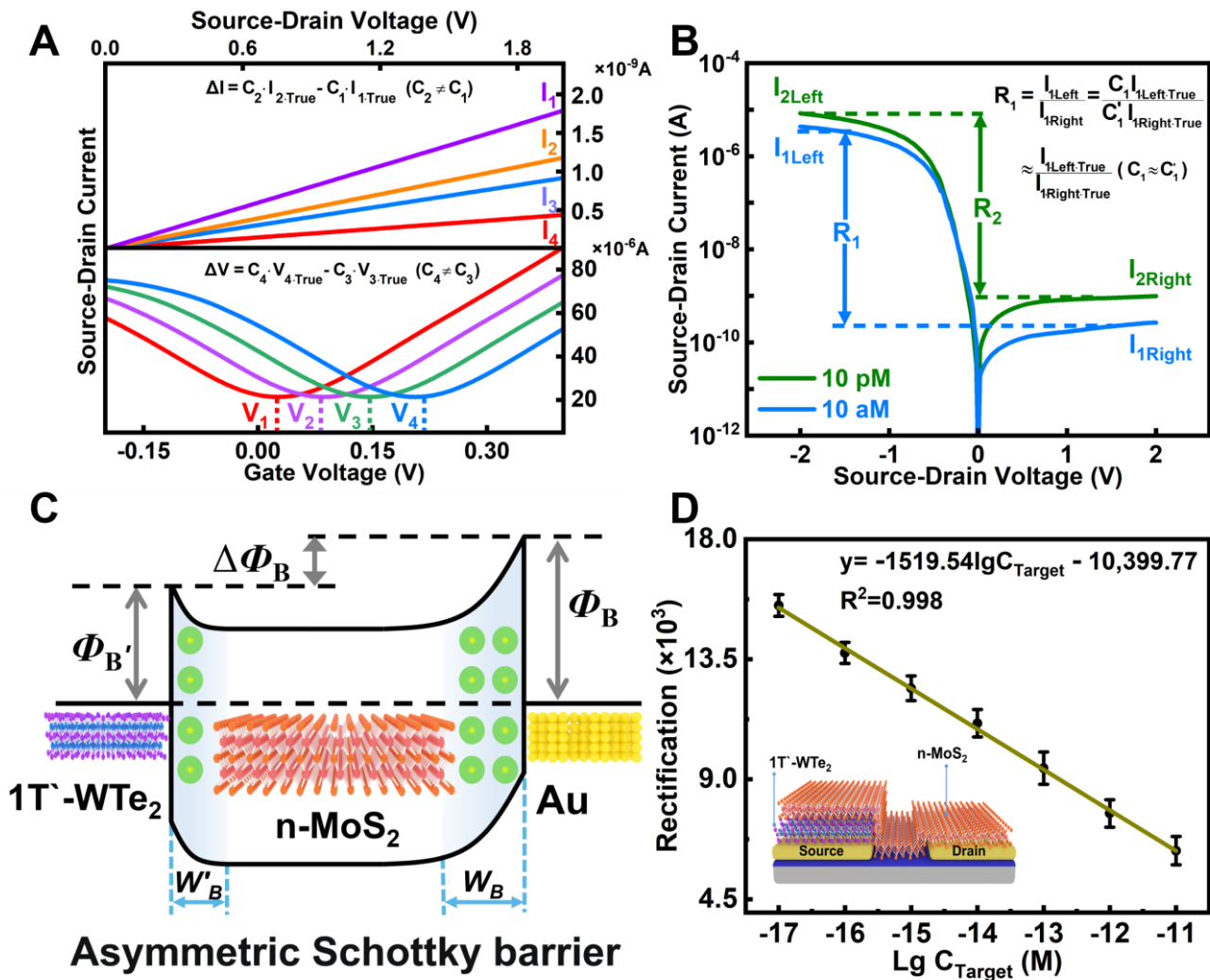


Figure 1. (A) Current–voltage images using the source-drain current, Dirac voltage, and other absolute value signals as response signals. (B) Current–voltage image when the rectification ratio, a rectified signal, is used as a response signal. (C) The band diagram of the structure generating the rectification ratio signal. (D) The linear relationship between the rectification ratio signal and the concentration of biomolecules. The inset shows a schematic diagram of the structure.

Figure 1B shows that, when the “rectified signal” is used as a response signal, the rectification ratio can be expressed as [20]:

$$\Delta R = R_2 - R_1, \tag{3}$$

where R_1 and R_2 are the rectification ratios at different biomolecular concentrations.

$$R_1 = \frac{I_{1\cdot\text{Left}}}{I_{1\cdot\text{Right}}} = \frac{C_1 \cdot I_{1\cdot\text{LeftTrue}}}{C_1' \cdot I_{1\cdot\text{RightTrue}}} \approx \frac{I_{1\cdot\text{LeftTrue}}}{I_{1\cdot\text{RightTrue}}} (C_1 \approx C_1'), \tag{4}$$

$$R_2 = \frac{I_{2\cdot\text{Left}}}{I_{2\cdot\text{Right}}} = \frac{C_2 \cdot I_{2\cdot\text{LeftTrue}}}{C_2' \cdot I_{2\cdot\text{RightTrue}}} \approx \frac{I_{2\cdot\text{LeftTrue}}}{I_{2\cdot\text{RightTrue}}} (C_2 \approx C_2'), \tag{5}$$

$I_{i\text{ Left}}$ ($i = 1,2$) and $I_{i\text{ Right}}$ are the source-drain currents under the sweep negative and positive voltages, respectively. Since $I_{i\text{ Left}}$ and $I_{i\text{ Right}}$ are measured at the same biomolecular concentration, they should be affected by external factors approximately equally ($C_i \approx C'_i$), which means that R_2 and R_1 values are approximately accurate. Thus, the variation in the “rectified signal” ($\Delta R = R_2 - R_1$) is approximately accurate. Using the “rectified signal” as a response signal accurately reflects the charge information carried by biomolecules.

A MoS₂/WTe₂ FET biosensor with an asymmetric Schottky barrier was constructed to measure the rectification ratio signal. Figure 1C shows the schematic diagram of its energy band structure. High-quality n-type MoS₂ and low-work function semimetal 1T'-WTe₂ were obtained by mechanical exfoliation and built into heterojunctions by a transfer platform [21]. In the MoS₂/WTe₂ FET biosensor, MoS₂ forms asymmetric Schottky junctions with 1T'-WTe₂ and Au, with barrier heights of Φ'_B and Φ_B and barrier widths of W'_B and W_B , respectively. The Schottky barrier height can be obtained from the Schottky–Mott relation [22]:

$$\Phi_B = \Phi_M - \chi_S, \quad (6)$$

where Φ_B is the Schottky barrier height, Φ_M is the work function of the metal electrodes, and χ_S represents the electron affinity of the n-type semiconductor. The Schottky barrier width can be obtained by the following formula [23]:

$$W = \sqrt{\frac{2\varepsilon_S V_{bi}}{qN_A}}, \quad (7)$$

where ε_S is the dielectric constant of the semiconductor; $V_{bi} = (\Phi_M - \Phi_S)/q$ is the built-in potential of the Schottky junction; q is the elementary charge; and N_A is the bulk charge density of the channel material.

Because of the lower work function of WTe₂ compared to that of Au, the Schottky barrier height and width of the MoS₂/Au junction is larger than those of the MoS₂/1T'-WTe₂ junction in the WTe₂/MoS₂/Au FET biosensor. The asymmetric Schottky barrier height between the two junctions leads to the generation of a rectification ratio signal in the heterojunction FET. As we know, the smaller the barrier width, the larger the tunneling current. In addition, the widths of the two junctions are different; thus, the smaller the W , the larger the tunneling current. Then, the tunneling currents of the two junctions are definitely not the same, which finally causes source-drain current changes at both ends, resulting in rectification ratio changes, as shown in Figure 1D.

3.2. Schematic Diagram of the MoS₂/WTe₂ FET Biosensor

The functionalization of the sensing surface, probe DNA immobilization, and target DNA hybridization were performed using the MoS₂/WTe₂ FET biosensor to generate a more stable response signal. In Figure 2A, 1-pyrenebutyric acid succinimidyl ester (PBASE) in the N,N-dimethylformamide solution was used as a linker between MoS₂ and the probe DNA, ensuring that the probe DNA could effectively bind to MoS₂ [24]. The pyrene group of PBASE was fixed on the MoS₂ surface by π - π stacking. The succinimide part of PBASE protruded from the MoS₂ surface and coupled with the amine group of the 5'-amine-modified DNA probe, as shown in Figure 2B [25]. Next, the target DNA complementary was added to the probe DNA. Consequently, the target DNA was hybridized with the probe DNA by base complementary pairing, as shown in Figure 2C. Notably, the different Schottky barrier widths of the MoS₂/WTe₂ FET biosensors can be obtained with the different steps, affecting the probability of tunneling current [26].

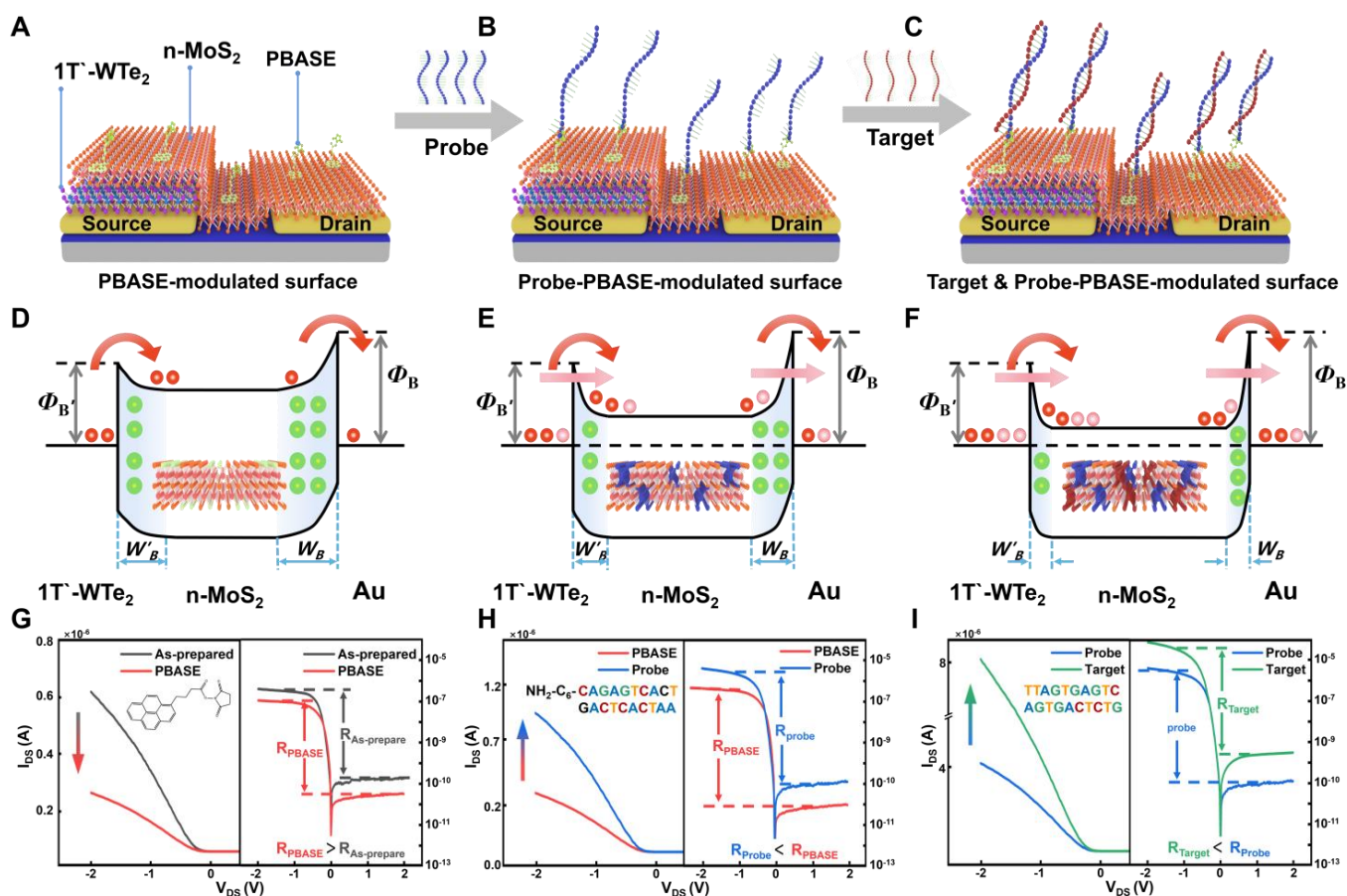


Figure 2. Schematic diagram of the MoS₂/WTe₂ FET biosensor. (A) Functionalization of the MoS₂/WTe₂ surface using the PBASE solution. (B) Immobilization of the probe DNA implied an interaction between PBASE and the probe DNA, achieving the binding of the probe DNA and the MoS₂/WTe₂ FET biosensor. (C) Interaction between the probe DNA and target DNA to form a double-stranded DNA. Schematic diagram of the band gap changes in the MoS₂/WTe₂ FET biosensor in the three processes: (D) functionalization of the sensing surface, (E) immobilization of the probe DNA, and (F) binding of the target DNA, where the charge injection mode modulated by PBASE on the surface is thermionic emission (TE), and the charge injection mode modulated by probe-PBASE on the surface and by target & probe-PBASE on the surface is tunneling. Absolute value signal I_{DS} (left) and rectified signal R (right) of the MoS₂/WTe₂ FET biosensor in the (G) functionalization, (H) immobilization of probe DNA, and (I) binding of target DNA.

In the functionalization process of MoS₂, the pyrene groups in PBASE fixed on the surface of MoS₂ by π - π stacking add a small amount of holes to the MoS₂/WTe₂ FET biosensor. Hole doping also effectively widens the Schottky barrier width of the MoS₂/WTe₂ FET biosensor. At this time, thermionic emission (TE) is the main charge injection mode, as shown in Figure 2D. That is to say, although the decrease in the forward bias current dominated by the MoS₂/Au junction is small, its relative decrease rate is larger, resulting in the increase in the rectification ratio R , as shown in Figure 2G. In the process of probe DNA immobilization, the succinimide part of the MoS₂ surface couples with the probe DNA, which fixes the probe DNA on MoS₂ and adds a small amount of electrons to the MoS₂/WTe₂ FET biosensor. Electron doping also effectively reduces the Schottky barrier width of the MoS₂/WTe₂ FET biosensor. At this time, the charge injection mode is electron tunneling and TE, as shown in Figure 2E. According to the conclusion, after fixing the probe DNA, the barrier width of the MoS₂/Au Schottky junction is reduced more and the relative current growth rate is higher than that of the MoS₂/1T'-WTe₂ Schottky junction. That is to

say, although the increase in the forward bias current dominated by the MoS₂/Au junction is small, its current growth rate is larger, resulting in the decrease in the rectification rate R , as shown in the right inset of Figure 2H. Similarly, target DNA hybridizes with probe DNA through base complementary pairing, which also adds electron doping to the MoS₂/WTe₂ FET biosensor. It increases the current and reduces the Schottky barrier width at the same time, and the barrier width of the MoS₂/Au junction is reduced more and the relative current growth rate is higher, resulting in the increase in the current and decrease in the rectification ratio R , as shown in Figure 2F,I.

The equation of the Schottky barrier width was used to calculate the change in the barrier width before and after doping. Their effects on the forward, reverse current, and rectification ratio signal were analyzed using Equations (2)–(4) [22]. The rectification ratio signal was found to effectively eliminate the interference of external factors on the molecular signal because it depends only on the ratio of the forward and reverse currents rather than the absolute value of the single-direction current. Therefore, the rectification ratio signal is not affected significantly, and an accurate expression of the charge information carried by biomolecules is obtained.

In addition, the rectification ratio signal not only reflects the changes in both Schottky junctions but also avoids the interference of the hysteresis phenomenon (Figure 2G–I). Since the forward and reverse source-drain currents are affected by the charge information on DNA molecules, the rectification ratio signal can detect weak charge information under the conditions of a low concentration DNA solution. In contrast, the forward or reverse source-drain current, which is used as the response signal, is difficult to separate from the noise signal [27], reducing the sensing sensitivity. Therefore, the rectification ratio signal as a kind of “response signal” is a promising biosensing signal, which can play a key role in biosensors and other sensing devices.

3.3. Structure and Characterization Analyses of the MoS₂/WTe₂ FET Biosensor

Figure 3A shows an optical image of the fabricated MoS₂/WTe₂ FET biosensor, consisting of a MoS₂/WTe₂ heterostructure and two electrodes on a SiO₂/Si substrate; the electrode spacing is 20 μm. Figure 3B shows the SEM image and the optical image of the area marked in Figure 3A. The corresponding EDS mapping of this area, showing the uniform distribution of each element [28], is shown in Figure S4. The EDS mapping shows that the atomic ratio of S to Mo in the MoS₂/WTe₂ FET biosensor is 2:1, and the atomic ratio of Te to W is 2:1, indicating the elements' uniform distribution. Figure 3C shows the image of the MoS₂/WTe₂ heterojunction measured by an atomic force microscope (AFM). The line scan profile of the heterojunction height was extracted from the AFM image, while the thicknesses of the MoS₂ and WTe₂ flakes were measured to be 5.72 nm and 20.41 nm. The Raman spectrum of the heterojunction (Figure 3D) was measured using a 532 nm laser. The Raman spectrum revealed the characteristic peak E_{2g}¹ representing the in-plane vibration mode was located at 383 cm⁻¹ and the characteristic peak A_{1g} representing the out-of-plane vibration mode was located at 407.79 cm⁻¹, consistent with the thickness of the MoS₂ flake [29,30]. The characteristic peaks ³A₂, ⁴A₁, ⁸A₁, and ¹⁰A₁ of WTe₂ were located near 116.4, 133.7, 163.9, and 211.8 cm⁻¹, respectively, consistent with the crystal structure of WTe₂ [31].

The electrical properties of MoS₂ and WTe₂ were measured [32]. Figure 3E shows the Schottky contact between the MoS₂ and Au electrodes and the Ohmic contact between the WTe₂ and Au electrodes. Figure 3F depicts the transfer characteristic curves of the MoS₂ and WTe₂ devices at a source-drain voltage V_{DS} = 0.5 V, where MoS₂ showed conventional n-type semiconductor characteristics [33] and the current of WTe₂ was unaffected by gate voltage, showing semimetal characteristics [34].

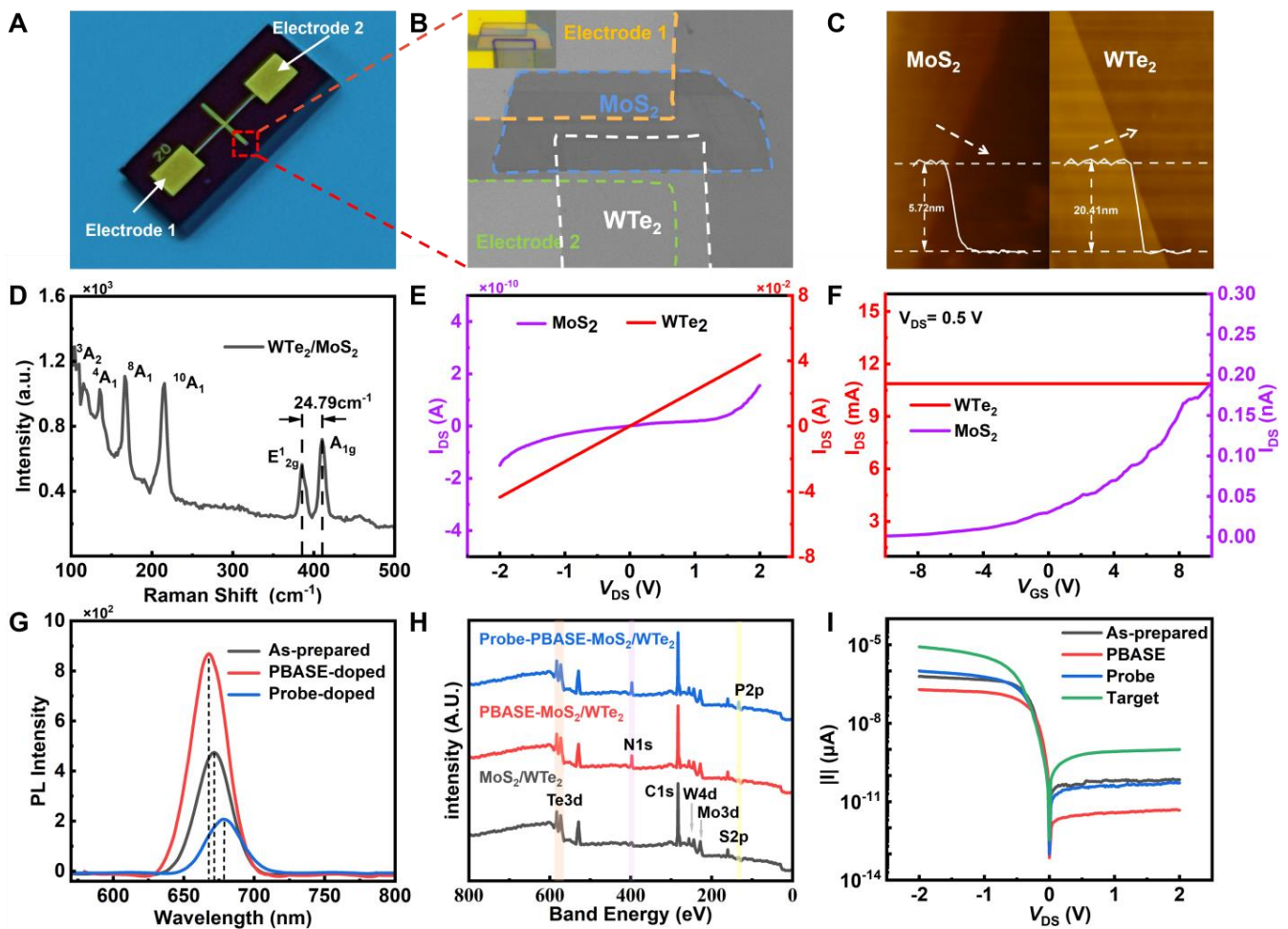


Figure 3. (A) A typical MoS₂/WTe₂ FET biosensor device. (B) SEM image of the MoS₂/WTe₂ FET biosensor, with its optical image in the inset. (C) AFM images of the MoS₂ and WTe₂ films. (D) Raman spectra of the MoS₂/WTe₂ heterojunction. (E,F) I_{DS} - V_{DS} and I_{DS} - V_{GS} characteristics of MoS₂ and WTe₂ at room temperature. The inset in (E) is the whole I_{DS} - V_{DS} characteristics of WTe₂. (G) Photoluminescence spectra with and without biomolecules. (H) X-ray photoelectron spectra before adding the target DYRK1A. (I) Current output characteristics after adding different biomolecules.

Photoluminescence (PL) and X-ray photoelectron spectroscopy (XPS) were used to verify that this biosensor can be successfully functionalized [35]. After functionalizing with MoS₂, the PL peak intensity increased, and the peak underwent a blue shift (See Figure 3G). After immobilizing the probe DNA, its PL peak intensity decreased, and the peak red-shifted. The peak intensity enhancement and the blue shift can be attributed to the following: The functionalized MoS₂ was affected by PBASE, where the electrons, trions A⁻, and foreign holes combined to form several neutral excitons A⁰, increasing the proportion of neutral excitons A⁰ and an enhancement in radiative transition. Consequently, the dominant exciton in the A peak changed from trion A⁻ to neutral exciton A⁰, leading to a PL peak intensity enhancement and the blue shift of the peak position. The peak intensity reduction and red shift can be attributed to the following: The immobilized MoS₂ was affected by the probe DNA, where foreign electrons and neutral excitons A⁰ combined to form trions A⁻. This was followed by the dominant exciton in the A peak changing from neutral exciton A⁰ to trion A⁻, while the radiative transition weakened, reducing the PL peak intensity and yielding the red shift of the peak position [36]. Figure 3H shows the N1s peak of PBASE and the P2p peak of the probe DNA, confirming the functionalization and immobilization of the probe DNA. The XPS measurements revealed that PBASE and the

probe DNA were successively bound to the MoS₂/WTe₂ surface. Furthermore, the change in the source-drain current in Figure 3I can be explained by the following reasoning: The adsorption of PBASE on the MoS₂/WTe₂ surface caused p-doping, resulting in a decrease in the overall source-drain current. The binding of the probe DNA with PBASE caused n-doping, increasing the source-drain current. Similarly, the complementary pairing of the target DNA with probe DNA caused n-doping, increasing the overall source-drain current [37,38].

3.4. Sensing Performance of the MoS₂/WTe₂ FET Biosensor

Down syndrome [39] is one of the most common chromosomal diseases and one of the main causes of human intellectual disability. The DYRK1A gene on chromosome 21 was chosen as the target DNA to study the sensitivity of the MoS₂/WTe₂ FET biosensor (Figure 4A). The functionalized and immobilized MoS₂/WTe₂ FET biosensor in different concentrations of the target DNA solution was studied to obtain the relationship between the target concentration and the response signal [40]. Figure 4B shows that the output characteristic curve gradually shifted upward as the concentration of the target DNA (DYRK1A) gradually increased from 10 aM to 100 pM. The current results of the different concentrations of the target DNA (DYRK1A) under positive and negative bias voltages are shown in Figure S5. Since the band gap width of MoS₂ was not zero [41], the noise signal of the MoS₂-based FET biosensor was much lower than that of the graphene FET biosensor [42,43]. When the target DNA concentration was as low as 10 aM, the detected source-drain current was much larger than that without adding the target DNA. Therefore, it can be confirmed that the 10 aM target DNA was successfully detected. Figure 4C shows the rectification ratio response with the increasing concentrations of the target DNA, which is attributed to the change in the Schottky barrier width caused by charge doping. Specifically, the change in the source-drain current dominated by the MoS₂/Au junction is larger than that dominated by the MoS₂/WTe₂ junction. Figure 4D shows that the rectification ratio gradually decreased as the concentration increased from 10 aM to 100 pM. Furthermore, the rectification ratio signal had a linear relationship with the concentration gradient ($y = -1519.54 \lg C_{\text{Target}} - 10,399.77$). These results indicate that the rectification ratio can serve as a kind of detection indicator in the MoS₂/WTe₂ FET biosensors.

Four kinds of biomarkers (N₁–N₄) diffused into the MoS₂/WTe₂ FET biosensor with the immobilized probe DNA were chosen to demonstrate the specificity of the MoS₂/WTe₂ FET biosensors. Figure 4E,F show that there is no obvious current change after adding 1 fM N₁–N₄ samples, and the inset of Figure 4E is the current after local magnification. The complete current diagram after adding the N₁–N₄ samples is shown in Figure S6. In addition, there is a higher response after adding the 10 aM target DNA than that after adding 1 fM N₁–N₄ samples. Figure 4F shows a comparison of the response ratios between the target DNA and non-target DNA samples, with N₁, N₂, N₃, and N₄ representing non-target DNA samples and P representing the target DNA sample. Thus, the proposed MoS₂/WTe₂ FET biosensor has a good specificity. As shown in Figure 4G, the biosensing performance of the MoS₂/WTe₂ FET biosensor did not decrease significantly after sixty days and the peak to valley value (PV) was still within an acceptable error range (PV = 9.86%). Thus, the MoS₂/WTe₂ FET biosensor demonstrated excellent stability and durability.

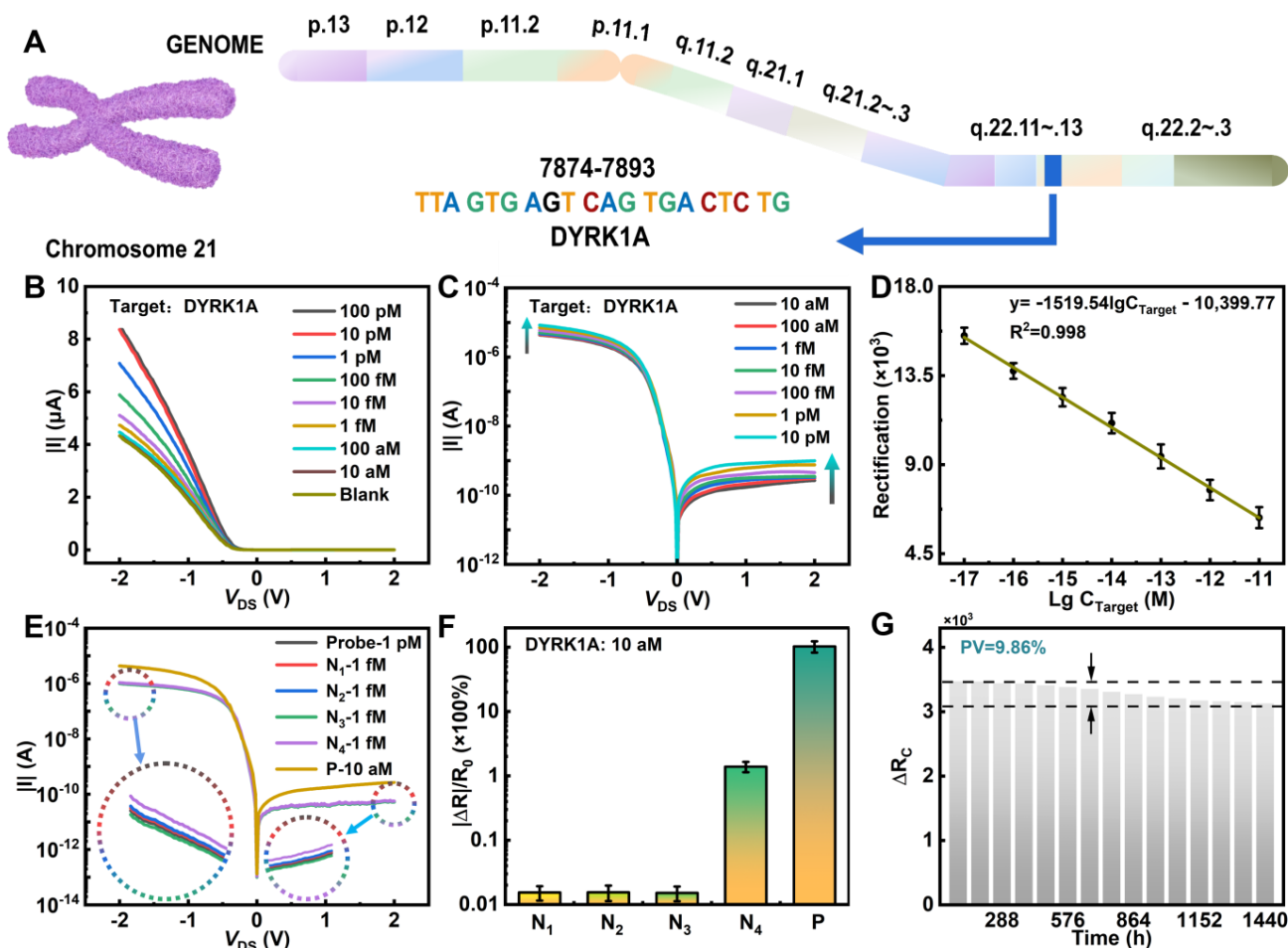


Figure 4. Sensing performance of the MoS₂/WTe₂ FET biosensor. (A) Target site of Down syndrome in chromosome 21 genome map. (B) Response of the output characteristic curve of the target DNA (DYRK1A gene). (C) Effect of the target DNA (DYRK1A gene) on the rectification ratio. (D) Statistics of the rectification ratio response of the DYRK1A gene. (E) Specificity response of the MoS₂/WTe₂ FET biosensor. (F) A comparison of the target DNA and non-target DNA. (G) The rectification ratio signal change values for the two concentrations during the sixty days; the peak to valley value is 9.87%.

3.5. Comparison of Similar Structures

The advantage of the “rectified signal” (rectification ratio) was demonstrated by constructing three kinds of FETs: Au/MoS₂/Au FET (Figure 5A), WTe₂/MoS₂/Au FET (Figure 5B), and WTe₂/MoS₂/WTe₂ FET (Figure 5C). Except for the reported WTe₂/MoS₂/Au FET, the other two FETs only showed “absolute value signal” (source-drain current) as the response signal. Due to the presence of a large symmetric barrier in Au/MoS₂/Au FET [44], the obtained current was about 1×10^{-10} A, as shown in Figure 5D. In contrast, due to the presence of an asymmetric barrier in WTe₂/MoS₂/Au FET, the forward source-drain current dominated by MoS₂/Au junction was about 1×10^{-10} A, while the reverse source-drain current dominated by WTe₂/MoS₂ junction was about 1×10^{-6} A (See Figure 5E). Furthermore, Figure 5F shows that, due to the presence of a symmetric small-barrier WTe₂/MoS₂/WTe₂ FET, the source-drain current was about 1×10^{-6} A. Figure S7 shows the changes in the transfer characteristic curves after introducing biomolecules in three different structures.

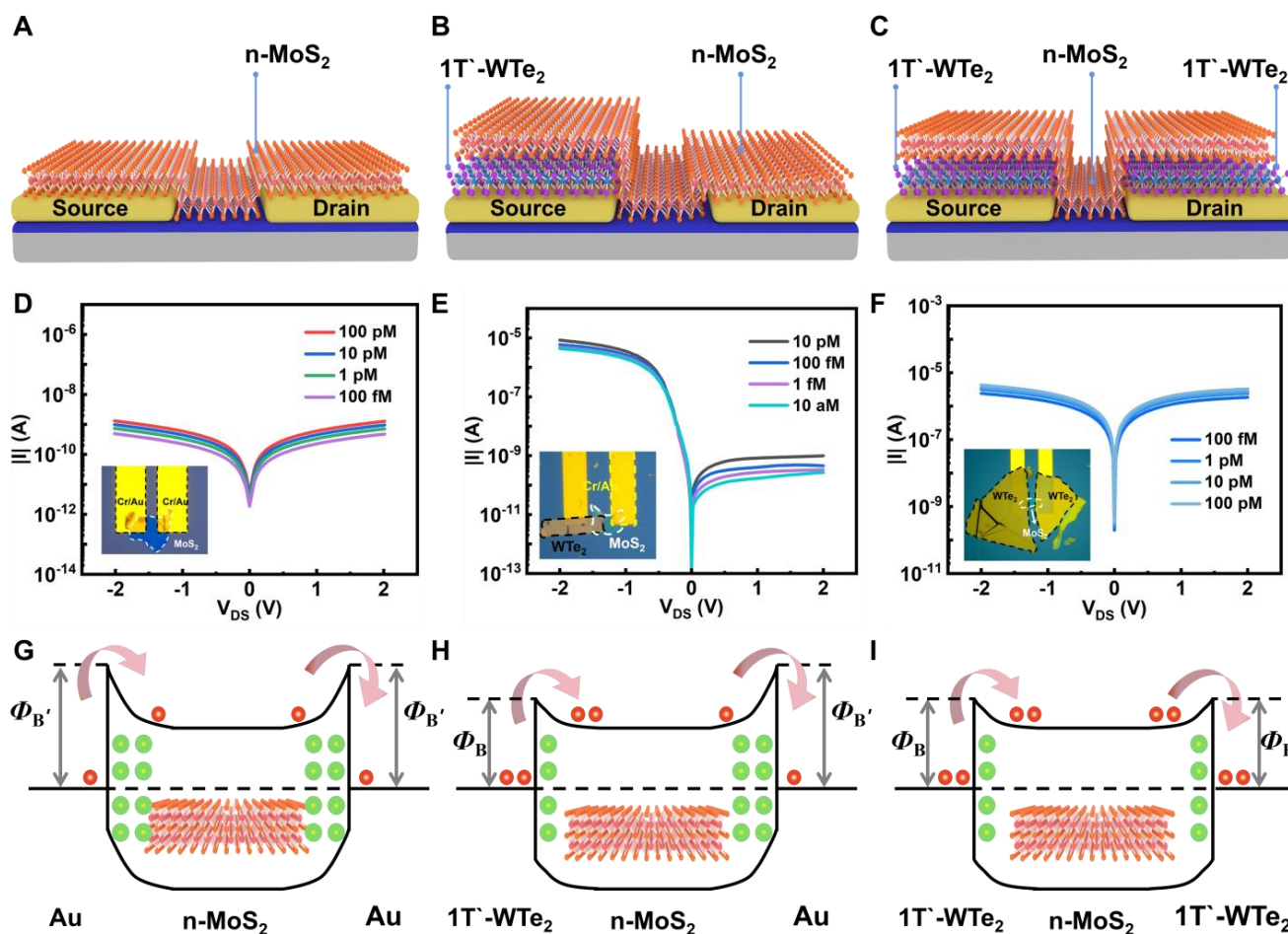


Figure 5. Comparison of similar structures. Schematic diagrams (A–C), output characteristic curves (D–F), and band diagrams (G–I) of the Au/MoS₂/Au, WTe₂/MoS₂/Au, and WTe₂/MoS₂/WTe₂ structures, respectively.

The source-drain current signals of the three structures were very weak, but the rectification ratio signal of the WTe₂/MoS₂/Au FET biosensor had significant variations. This indicates that the rectification ratio signal effectively amplifies the molecular signal variation and improves molecular signal sensitivity. Figure 5G–I shows the band diagram of the three structures. When the target biomolecules modified the sensing materials, the Schottky barrier widths were modulated. As shown in Figure 5G, when the target DNA caused electron doping [22], the Schottky barrier width of the MoS₂/Au junction decreased and the source-drain current increased. As shown in Figure 5H, the asymmetric barrier decreased after adding the target DNA, resulting in an increased current and a decreased rectification ratio (Figure S8). Figure 5I shows that, when the target DNA was added into WTe₂/MoS₂/WTe₂ FET, it caused electron doping and decreased the Schottky barrier width, increasing the source-drain current.

Moreover, the rectification ratio signal of the WTe₂/MoS₂/Au FET biosensor is stable for long periods of time (Figure S9), indicating that the “rectified signal” (the rectification ratio) is not affected by the solution environment and is a promising biosensing signal in FET biosensors.

4. Conclusions

This study developed a novel strategy using the “rectified signal” in the output characteristic curve to detect biomolecules. The strategy effectively avoided the interference of external factors and was suitable for the quantitative analysis of trace targets in com-

plex biological systems. Based on this strategy, a highly reliable and stable MoS₂/WTe₂ FET biosensor with an asymmetric Schottky barrier was developed. The experiments showed that the prepared biosensor achieved an ultra-sensitive and specific detection of the DYRK1A gene in the range of 10 aM–100 pM, indicating that the MoS₂/WTe₂ FET biosensor has great application potential in the prenatal screening of Down syndrome. This study demonstrated the importance of using a “rectified signal” in FET biosensors and provided a novel perspective for designing and optimizing biosensors based on two-dimensional materials.

Supplementary Materials: The following supporting information can be downloaded at: <https://www.mdpi.com/article/10.3390/nano14020226/s1>. Figure S1: Fabrication process diagram of the MoS₂/WTe₂ FET biosensor; Figure S2: The functionalization and immobilization process of the device; Figure S3: High-resolution XPS spectra of Mo 3d and S 2p; Figure S4: EDS images mentioned in Figure 3B; Figure S5: The current results of different concentrations of the target DNA (DYRK1A) under (A) positive and (B) negative bias voltages; Figure S6: The complete current diagram after adding the N₁–N₄ samples; Figure S7: The transfer characteristic curves of the Au/MoS₂/Au, WTe₂/MoS₂/Au, and WTe₂/MoS₂/WTe₂ structures; Figure S8: Output characteristic curves measured at different biomolecular concentrations in the MoS₂/WTe₂ FET biosensor; Figure S9: Stability comparison of the “rectified signal” and “absolute value signal”; Table S1: The DNA sequences purchased from Sangon Biotech (Shanghai) Co., Ltd.; Table S2: Comparison of the biosensing performances of the various FET biosensors. References [45–52] are cited in the supplementary materials.

Author Contributions: Conceptualization, X.Z. and S.C.; methodology, H.M.; software, T.S.; validation, X.Z., S.C. and H.M.; formal analysis, T.S.; investigation, X.C.; resources, S.C.; data curation, P.H.; writing—original draft preparation, X.Z.; writing—review and editing, C.Y.; visualization, C.Y.; supervision, B.M.; project administration, B.M.; funding acquisition, C.Y. All authors have read and agreed to the published version of the manuscript.

Funding: This research was funded by the National Natural Science Foundation of China (11974222) and the Shandong Provincial Natural Science Foundation (ZR2023MA087).

Data Availability Statement: Data are contained within the article and Supplementary Materials.

Acknowledgments: The authors acknowledge the anonymous referees for their helpful comments and constructive remarks on this manuscript.

Conflicts of Interest: The authors declare no conflicts of interest.

References

1. Wang, L.; Wang, X.; Wu, Y.; Guo, M.; Gu, C.; Dai, C.; Kong, D.; Wang, Y.; Zhang, C.; Qu, D. Rapid and ultrasensitive electromechanical detection of ions, biomolecules and SARS-CoV-2 RNA in unamplified samples. *Nat. Biomed. Eng.* **2022**, *6*, 276–285. [[CrossRef](#)]
2. Wang, C.; Li, W.; Drabek, D.; Okba, N.M.; van Haperen, R.; Osterhaus, A.D.; van Kuppeveld, F.J.; Haagmans, B.L.; Grosveld, F.; Bosch, B.-J. A human monoclonal antibody blocking SARS-CoV-2 infection. *Nat. Commun.* **2020**, *11*, 2251. [[CrossRef](#)]
3. Ji, H.; Wang, Z.; Wang, S.; Wang, C.; Chu, Y.; Liu, H.; Zhang, Y.; Han, L. A Novel InSe-FET Biosensor based on Carrier-Scattering Regulation Derived from the DNA Probe Assembly-Determined Electrostatic Potential Distribution. *Adv. Funct. Mater.* **2023**, *33*, 2213277. [[CrossRef](#)]
4. von Lüders, L.; Tilmann, R.; Lee, K.; Bartlam, C.; Stimpel-Lindner, T.; Nevanen, T.K.; Iljin, K.; Knirsch, K.C.; Hirsch, A.; Duesberg, G.S. Functionalisation of Graphene Sensor Surfaces for the Specific Detection of Biomarkers. *Angew. Chem. Int. Ed.* **2023**, *62*, e202219024. [[CrossRef](#)] [[PubMed](#)]
5. Gilpatrick, T.; Lee, I.; Graham, J.E.; Raimondeau, E.; Bowen, R.; Heron, A.; Downs, B.; Sukumar, S.; Sedlazeck, F.J.; Timp, W. Targeted nanopore sequencing with Cas9-guided adapter ligation. *Nat. Biotechnol.* **2020**, *38*, 433–438. [[CrossRef](#)]
6. Li, B.; Deng, A.; Li, K.; Hu, Y.; Li, Z.; Shi, Y.; Xiong, Q.; Liu, Z.; Guo, Q.; Zou, L. Viral infection and transmission in a large, well-traced outbreak caused by the SARS-CoV-2 Delta variant. *Nat. Commun.* **2022**, *13*, 460. [[CrossRef](#)]
7. Zhang, X.; Liu, T.; Boyle, A.; Bahreman, A.; Bao, L.; Jing, Q.; Xue, H.; Kielyka, R.; Kros, A.; Schneider, G.F. Dielectric-Modulated Biosensing with Ultrahigh-Frequency-Operated Graphene Field-Effect Transistors. *Adv. Mater.* **2022**, *34*, 2270055. [[CrossRef](#)]
8. Jiang, J.; Chu, Z.; Yin, Z.; Li, J.; Yang, Y.; Chen, J.; Wu, J.; You, J.; Zhang, X. Red Perovskite Light-Emitting Diodes with Efficiency Exceeding 25% Realized by Co-Spacer Cations. *Adv. Mater.* **2022**, *34*, 2204460. [[CrossRef](#)]
9. Hou, S.; Wu, M.; Li, H.; Gong, H.R.; Gao, Z.; Shi, R.; Huang, X.; Li, D.; Huang, J.D.; Yu, J. Ultrasensitive Detection of SARS-CoV-2 by Flexible Metal Oxide Field-Effect Transistors. *Adv. Funct. Mater.* **2023**, *33*, 2301268. [[CrossRef](#)]

10. Sen, A.; Shim, J.; Bala, A.; Park, H.; Kim, S. Boosting Sensitivity and Reliability in Field-Effect Transistor-Based Biosensors with Nanoporous MoS₂ Encapsulated by Non-Planar Al₂O₃. *Adv. Funct. Mater.* **2023**, *33*, 2301919. [[CrossRef](#)]
11. Kulkarni, G.S.; Zhong, Z. Detection beyond the Debye screening length in a high-frequency nanoelectronic biosensor. *Nano Lett.* **2012**, *12*, 719–723. [[CrossRef](#)]
12. Sadighbayan, D.; Hasanzadeh, M.; Ghafar-Zadeh, E. Biosensing based on field-effect transistors (FET): Recent progress and challenges. *TrAC Trends Anal. Chem.* **2020**, *133*, 116067. [[CrossRef](#)] [[PubMed](#)]
13. Xu, S.; Zhan, J.; Man, B.; Jiang, S.; Yue, W.; Gao, S.; Guo, C.; Liu, H.; Li, Z.; Wang, J. Real-time reliable determination of binding kinetics of DNA hybridization using a multi-channel graphene biosensor. *Nat. Commun.* **2017**, *8*, 14902. [[CrossRef](#)] [[PubMed](#)]
14. Di Bartolomeo, A.; Kumar, A.; Durante, O.; Sessa, A.; Faella, E.; Viscardi, L.; Intonti, K.; Giubileo, F.; Martucciello, N.; Romano, P. Temperature-dependent photoconductivity in two-dimensional MoS₂ transistors. *Mater. Today Nano* **2023**, *24*, 100382. [[CrossRef](#)]
15. Fathi-Hafshejani, P.; Azam, N.; Wang, L.; Kuroda, M.A.; Hamilton, M.C.; Hasim, S.; Mahjouri-Samani, M. Two-dimensional-material-based field-effect transistor biosensor for detecting COVID-19 virus (SARS-CoV-2). *ACS Nano* **2021**, *15*, 11461–11469. [[CrossRef](#)]
16. Chen, S.; Sun, Y.; Xia, Y.; Lv, K.; Man, B.; Yang, C. Donor effect dominated molybdenum disulfide/graphene nanostructure-based field-effect transistor for ultrasensitive DNA detection. *Biosens. Bioelectron.* **2020**, *156*, 112128. [[CrossRef](#)]
17. Hajian, R.; Balderston, S.; Tran, T.; DeBoer, T.; Etienne, J.; Sandhu, M.; Wauford, N.A.; Chung, J.-Y.; Nokes, J.; Athaiya, M. Detection of unamplified target genes via CRISPR–Cas9 immobilized on a graphene field-effect transistor. *Nat. Biomed. Eng.* **2019**, *3*, 427–437. [[CrossRef](#)] [[PubMed](#)]
18. Balderston, S.; Taulbee, J.J.; Celaya, E.; Fung, K.; Jiao, A.; Smith, K.; Hajian, R.; Gasiunas, G.; Kutanovas, S.; Kim, D. Discrimination of single-point mutations in unamplified genomic DNA via Cas9 immobilized on a graphene field-effect transistor. *Nat. Biomed. Eng.* **2021**, *5*, 713–725. [[CrossRef](#)]
19. Mei, J.; Li, Y.-T.; Zhang, H.; Xiao, M.-M.; Ning, Y.; Zhang, Z.-Y.; Zhang, G.-J. Molybdenum disulfide field-effect transistor biosensor for ultrasensitive detection of DNA by employing morpholino as probe. *Biosens. Bioelectron.* **2018**, *110*, 71–77. [[CrossRef](#)]
20. Hu, S.; An, M.; Yang, N.; Li, B. A series circuit of thermal rectifiers: An effective way to enhance rectification ratio. *arXiv* **2016**, arXiv:1605.01806. [[CrossRef](#)]
21. Zhao, Q.; Jie, W.; Wang, T.; Castellanos-Gomez, A.; Frisenda, R. InSe Schottky diodes based on van der Waals contacts. *Adv. Funct. Mater.* **2020**, *30*, 2001307. [[CrossRef](#)]
22. Zhang, X.; Liu, B.; Gao, L.; Yu, H.; Liu, X.; Du, J.; Xiao, J.; Liu, Y.; Gu, L.; Liao, Q. Near-ideal van der Waals rectifiers based on all-two-dimensional Schottky junctions. *Nat. Commun.* **2021**, *12*, 1522. [[CrossRef](#)] [[PubMed](#)]
23. Li, B.; Xing, T.; Zhong, M.; Huang, L.; Lei, N.; Zhang, J.; Li, J.; Wei, Z. A two-dimensional Fe-doped SnS₂ magnetic semiconductor. *Nat. Commun.* **2017**, *8*, 1958. [[CrossRef](#)] [[PubMed](#)]
24. Khosravi, F.; Loeian, S.M.; Panchapakesan, B. Ultrasensitive label-free sensing of IL-6 based on PASE functionalized carbon nanotube micro-arrays with RNA-aptamers as molecular recognition elements. *Biosensors* **2017**, *7*, 17. [[CrossRef](#)]
25. Hwang, C.; Park, N.; Kim, E.S.; Kim, M.; Kim, S.D.; Park, S.; Kim, N.Y.; Kim, J.H. Ultra-fast and recyclable DNA biosensor for point-of-care detection of SARS-CoV-2 (COVID-19). *Biosens. Bioelectron.* **2021**, *185*, 113177. [[CrossRef](#)]
26. Tan, C.; Yin, S.; Chen, J.; Lu, Y.; Wei, W.; Du, H.; Liu, K.; Wang, F.; Zhai, T.; Li, L. Broken-gap PtS₂/WSe₂ van der Waals heterojunction with ultrahigh reverse rectification and fast photoresponse. *ACS Nano* **2021**, *15*, 8328–8337. [[CrossRef](#)]
27. Le, V.X.; Lee, H.; Pham, N.S.; Bong, S.; Oh, H.; Cho, S.-H.; Shin, I.-S. Stainless steel 304 needle electrode for precise glucose biosensor with high signal-to-noise ratio. *Sens. Actuators B Chem.* **2021**, *346*, 130552. [[CrossRef](#)]
28. Mao, J.; Zhang, B.; Shi, Y.; Wu, X.; He, Y.; Wu, D.; Jie, J.; Lee, C.S.; Zhang, X. Conformal MoS₂/silicon nanowire array heterojunction with enhanced light trapping and effective interface passivation for ultraweak infrared light detection. *Adv. Funct. Mater.* **2022**, *32*, 2108174. [[CrossRef](#)]
29. Zhang, D.; Yang, Z.; Li, P.; Pang, M.; Xue, Q. Flexible self-powered high-performance ammonia sensor based on Au-decorated MoSe₂ nanoflowers driven by single layer MoS₂-flake piezoelectric nanogenerator. *Nano Energy* **2019**, *65*, 103974. [[CrossRef](#)]
30. Li, H.; Zhang, Q.; Yap, C.C.R.; Tay, B.K.; Edwin, T.H.T.; Olivier, A.; Baillargeat, D. From bulk to monolayer MoS₂: Evolution of Raman scattering. *Adv. Funct. Mater.* **2012**, *22*, 1385–1390. [[CrossRef](#)]
31. Wei, Y.; Deng, C.; Zheng, X.; Chen, Y.; Zhang, X.; Luo, W.; Zhang, Y.; Peng, G.; Liu, J.; Huang, H. Anisotropic in-plane thermal conductivity for multi-layer WTe₂. *Nano. Res.* **2022**, *15*, 401–407. [[CrossRef](#)]
32. Chen, Y.; Liu, H.; Yu, G.; Ma, C.; Xu, Z.; Zhang, J.; Zhang, C.; Chen, M.; Li, D.; Zheng, W. Defect Engineering of 2D Semiconductors for Dual Control of Emission and Carrier Polarity. *Adv. Mater.* **2023**, e2312425. [[CrossRef](#)] [[PubMed](#)]
33. Kumar, A.; Viscardi, L.; Faella, E.; Giubileo, F.; Intonti, K.; Pelella, A.; Sleziona, S.; Kharsah, O.; Schleberger, M.; Di Bartolomeo, A. Black phosphorus unipolar transistor, memory, and photodetector. *J. Mater. Sci.* **2023**, *58*, 2689–2699. [[CrossRef](#)]
34. Zhou, C.; Raju, S.; Li, B.; Chan, M.; Chai, Y.; Yang, C.Y. Self-driven metal–semiconductor–metal WSe₂ photodetector with asymmetric contact geometries. *Adv. Funct. Mater.* **2018**, *28*, 1802954. [[CrossRef](#)]
35. Sheta, S.M.; El-Sheikh, S.M.; Abd-Elzaher, M.M.; Salem, S.R.; Moussa, H.A.; Mohamed, R.M.; Mkhallid, I.A. A novel biosensor for early diagnosis of liver cancer cases using smart nano-magnetic metal–organic framework. *Appl. Organomet. Chem.* **2019**, *33*, e5249. [[CrossRef](#)]
36. Mouri, S.; Miyauchi, Y.; Matsuda, K. Tunable photoluminescence of monolayer MoS₂ via chemical doping. *Nano Lett.* **2013**, *13*, 5944–5948. [[CrossRef](#)] [[PubMed](#)]

37. Rabchinskii, M.K.; Saveliev, S.D.; Stolyarova, D.Y.; Brzhezinskaya, M.; Kirilenko, D.A.; Baidakova, M.V.; Ryzhkov, S.A.; Shnitov, V.V.; Sysoev, V.V.; Brunkov, P.N. Modulating nitrogen species via N-doping and post annealing of graphene derivatives: XPS and XAS examination. *Carbon* **2021**, *182*, 593–604. [[CrossRef](#)]
38. Taklu, B.W.; Su, W.-N.; Nikodimos, Y.; Lakshmanan, K.; Temesgen, N.T.; Lin, P.-X.; Jiang, S.-K.; Huang, C.-J.; Wang, D.-Y.; Sheu, H.-S. Dual CuCl doped argyrodite superconductor to boost the interfacial compatibility and air stability for all solid-state lithium metal batteries. *Nano Energy* **2021**, *90*, 106542. [[CrossRef](#)]
39. Hüls, A.; Costa, A.C.; Dierssen, M.; Baksh, R.A.; Bargagna, S.; Baumer, N.T.; Brandão, A.C.; Carfi, A.; Carmona-Iragui, M.; Chicoine, B.A. Medical vulnerability of individuals with Down syndrome to severe COVID-19—data from the Trisomy 21 Research Society and the UK ISARIC4C survey. *EClinicalMedicine* **2021**, *33*, 100769. [[CrossRef](#)]
40. Wang, S.; Sun, M.; Zhang, Y.; Ji, H.; Gao, J.; Song, S.; Sun, J.; Liu, H.; Zhang, Y.; Han, L. Ultrasensitive antibiotic perceiving based on aptamer-functionalized ultraclean graphene field-effect transistor biosensor. *Anal. Chem.* **2022**, *94*, 14785–14793. [[CrossRef](#)]
41. Mak, K.F.; Lee, C.; Hone, J.; Shan, J.; Heinz, T.F. Atomically thin MoS₂: A new direct-gap semiconductor. *Phys. Rev. Lett.* **2010**, *105*, 136805. [[CrossRef](#)] [[PubMed](#)]
42. Song, P.; Ou, P.; Wang, Y.; Yuan, H.; Duan, S.; Chen, L.; Fu, H.; Song, J.; Liu, X. An ultrasensitive FET biosensor based on vertically aligned MoS₂ nanolayers with abundant surface active sites. *Anal. Chim. Acta* **2023**, *1252*, 341036. [[CrossRef](#)] [[PubMed](#)]
43. Marconcini, P.; Macucci, M. Envelope-function-based transport simulation of a graphene ribbon with an antidot lattice. *IEEE Trans. Nanotechnol.* **2016**, *16*, 534–544. [[CrossRef](#)]
44. Liu, J.; Hao, Q.; Gan, H.; Li, P.; Li, B.; Tu, Y.; Zhu, J.; Qi, D.; Chai, Y.; Zhang, W. Selectively Modulated Photoresponse in Type-I Heterojunction for Ultrasensitive Self-Powered Photodetectors. *Laser-Photon. Rev.* **2022**, *16*, 2200338. [[CrossRef](#)]
45. Khan, N.I.; Mousazadehkasin, M.; Ghosh, S.; Tsavalas, J.G.; Song, E. An integrated microfluidic platform for selective and real-time detection of thrombin biomarkers using a graphene FET. *Analyst* **2020**, *145*, 4494–4503. [[CrossRef](#)]
46. Park, D.; Kim, J.H.; Kim, H.J.; Lee, D.; Lee, D.S.; Yoon, D.S.; Hwang, K.S. Multiplexed femtomolar detection of Alzheimer’s disease biomarkers in biofluids using a reduced graphene oxide field-effect transistor. *Biosens. Bioelectron.* **2020**, *167*, 112505. [[CrossRef](#)]
47. Danielson, E.; Sontakke, V.A.; Porkovich, A.J.; Wang, Z.; Kumar, P.; Ziadi, Z.; Yokobayashi, Y.; Sowwan, M. Graphene based field-effect transistor biosensors functionalized using gas-phase synthesized gold nanoparticles. *Sens. Actuators B Chem.* **2020**, *320*, 128432. [[CrossRef](#)]
48. Li, Y.; Peng, Z.; Holl, N.J.; Hassan, M.R.; Pappas, J.M.; Wei, C.; Izadi, O.H.; Wang, Y.; Dong, X.; Wang, C. MXene–graphene field-effect transistor sensing of influenza virus and SARS-CoV-2. *ACS Omega* **2021**, *6*, 6643–6653. [[CrossRef](#)]
49. Park, H.; Lee, H.; Jeong, S.H.; Lee, E.; Lee, W.; Liu, N.; Yoon, D.S.; Kim, S.; Lee, S.W. MoS₂ field-effect transistor-amyloid-β1–42 hybrid device for signal amplified detection of MMP-9. *Anal. Chem.* **2019**, *91*, 8252–8258. [[CrossRef](#)]
50. Liu, J.; Chen, X.; Wang, Q.; Xiao, M.; Zhong, D.; Sun, W.; Zhang, G.; Zhang, Z. Ultrasensitive monolayer MoS₂ field-effect transistor based DNA sensors for screening of down syndrome. *Nano Lett.* **2019**, *19*, 1437–1444. [[CrossRef](#)]
51. Chan, C.; Shi, J.; Fan, Y.; Yang, M. A microfluidic flow-through chip integrated with reduced graphene oxide transistor for influenza virus gene detection. *Sens. Actuators B Chem.* **2017**, *251*, 927–933. [[CrossRef](#)]
52. Islam, S.; Shukla, S.; Bajpai, V.K.; Han, Y.-K.; Huh, Y.S.; Kumar, A.; Ghosh, A.; Gandhi, S. A smart nanosensor for the detection of human immunodeficiency virus and associated cardiovascular and arthritis diseases using functionalized graphene-based transistors. *Biosens. Bioelectron.* **2019**, *126*, 792–799. [[CrossRef](#)] [[PubMed](#)]

Disclaimer/Publisher’s Note: The statements, opinions and data contained in all publications are solely those of the individual author(s) and contributor(s) and not of MDPI and/or the editor(s). MDPI and/or the editor(s) disclaim responsibility for any injury to people or property resulting from any ideas, methods, instructions or products referred to in the content.